Supplementary information

Reversible colossal barocaloric effect dominated by disordering of organic chains in (CH₃-(CH₂)ₙ₋₁-NH₃)₂MnCl₄ single crystals

Yihong Gao*[1,2], Hongxiong Liu*[1,2], Fengxia Hu[1,2,3], Hongyan Song[1,2], Hao Zhang[1,2], Jiazheng Hao[1], Xingzheng Liu[1,2], Zibing Yu[1,2], Feiran Shen[1], Yangxin Wang[1,2], Houbo Zhou[1,2], Bingjie Wang[1,2], Zhengying Tian[1,2], Yuan Lin[1,2], Cheng Zhang[1,2], Zhuo Yin[1,2], Jing Wang[1,2,4], Yunzhong Chen[1], Yunliang Li[1,2,3], Youting Song[1], Youguo Shi[1,2,3], Tongyun Zhao[1,5], Jirong Sun[1,2,3], Qingzhen Huang[6], and Baogen Shen[1,2,3,7]

[1]Beijing National Laboratory for Condensed Matter physics, Institute of Physics, Chinese Academy of Sciences, Beijing 100190, P. R. China.

[2]School of Physical Sciences, University of Chinese Academy of Sciences, Beijing 101408, China.

[3]Songshan Lake Materials Laboratory, Dongguan, Guangdong 523808, P. R. China.

[4]Fujian Innovation Academy, Chinese Academy of Sciences, Fuzhou, Fujian 350108, China.

[5]Ganjiang Innovation Academy, Chinese Academy of Sciences, Ganzhou, Jiangxi 341000, China.

[6]NIST Center for Neutron Research, National Institute of Standards and Technology, Gaithersburg, Maryland 20899, USA.

[7]Ningbo Institute of Materials Technology & Engineering, Chinese Academy of Sciences, Ningbo, Zhejiang 315201, China.

*These authors contributed equally to this work.

Corresponding authors:
Fengxia Hu   E-mail: fxhu@iphy.ac.cn
Jing Wang   E-mail: wangjing@iphy.ac.cn
Yunliang Li   E-mail: yunliangli@iphy.ac.cn
Baogen Shen   E-mail: shenbg@iphy.ac.cn

This supplementary information consists of 7 sections. SI-1 presents the SC-XRD diffraction images of (CH₃-(CH₂)ₙ₋₁-NH₃)₂MnCl₄(n=9, 10). SI-2 and SI-3 present the complete information of SC-XRD and FT-IR results on (CH₃-(CH₂)ₙ₋₁-NH₃)₂MnCl₄ (n=10). SI-4, SI-5 and SI-6 present the details of barocaloric characterization on (CH₃-(CH₂)ₙ₋₁-NH₃)₂MnCl₄(n=9,10). SI-7 discusses additional barocaloric effect in (CH₃-(CH₂)ₙ₋₁-NH₃)₂MnCl₄(n=10).

Series title:
SI-1. Diffraction images of (CH₃-(CH₂)ₙ₋₁-NH₃)₂MnCl₄ (n=9, 10)
SI-2. Single-crystal XRD measurements of (CH₃-(CH₂)ₙ₋₁-NH₃)₂MnCl₄ (n=10)

SI-3. Fourier transform infrared spectroscopy measurements of $(CH_3-(CH_2)_{n-1}-NH_3)_2MnCl_4$ (n=10)

SI-4. Barocaloric characterization on $(CH_3-(CH_2)_{n-1}-NH_3)_2MnCl_4$ (n=9)

SI-5. Characterization of barocaloric performance by quasi-direct method

SI-6. Specific heat capacity of $(CH_3-(CH_2)_{n-1}-NH_3)_2MnCl_4$ (n=9, 10)

SI-7. Additional barocaloric effect in $(CH_3-(CH_2)_{n-1}-NH_3)_2MnCl_4$ (n=10)

SI-1. Diffraction images of $(CH_3-(CH_2)_{n-1}-NH_3)_2MnCl_4$ (n=9,10)

The compared diffraction images of $(CH_3-(CH_2)_{n-1}-NH_3)_2MnCl_4$ (n=9,10) obtained by SC-XRD are shown below.
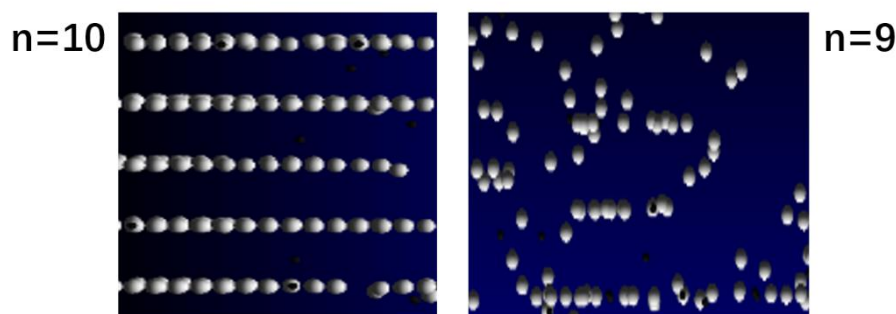

Fig. S1. Compared SC-XRD diffraction images for n=10 single crystal (left) and the n=9 sample with partial lattice stacking order (right).

SI-2. Single-crystal XRD measurements of $(CH_3-(CH_2)_{n-1}-NH_3)_2MnCl_4$ (n=10)

SC-XRD results demonstrate that at 298 K of low-temperature phase, $(CH_3-(CH_2)_{n-1}-NH_3)_2MnCl_4$ (n=10) adopts monoclinic space group $P2_1/c$, with two molecules in lattice cell and cell constants of a=26.698 Å, b=7.3359 Å, c=7.2052 Å, β=94.39°. When heating up to 308 K of low-temperature phase, $(CH_3-(CH_2)_{n-1}-NH_3)_2MnCl_4$ (n=10) still adopts same space group $P2_1/c$ with two molecules in one unit cell, but lattice expanded due to heating, with cell constants of a=26.791 Å, b=7.3473 Å, c=7.2116 Å, β=94.297°. Further, when continuously heating to 320 K of high-temperature phase, single crystal XRD demonstrates that the crystal adopts tetragonal space group P4/mmm with cell constants of a=b=5.154 Å, c=28.340 Å, meanwhile the information of organic chains disappears under the gaze of X-ray owe to the broken spatial translation symmetry caused by disorder of organic moieties. As seen in Fig. S2, Fig. S3, and Fig. S4, we marked the atomic sequence in $(CH_3-(CH_2)_{n-1}-NH_3)_2MnCl_4$ (n=10) at 298 K, 308 K and 320 K, respectively, by which Table S4, Table S5, and Table S6 show the bond angles at 298 K, 308 K and 320 K.

Table S1. Data collection and structure refinement for $(CH_3\text{-}(CH_2)_9\text{-}NH_3)_2MnCl_4$ at 298 K.

Theta range for data collection	0.77 to 28.28°
Index ranges	-34<=h<=35, -9<=k<=9, -9<=l<=9
Reflections collected	12484
Independent reflections	3470 [R(int) = 0.0782]
Coverage of independent reflections	99.4%
Absorption correction	Multi-Scan
Structure solution technique	direct methods
Structure solution program	XT, VERSION 2014/5
Refinement method	Full-matrix least-squares on F^2
Refinement program	SHELXL-2014/7 (Sheldrick, 2014)
Function minimized	$\Sigma\ w(F_o^2 - F_c^2)^2$
Data / restraints / parameters	3470 / 9 / 134
Goodness-of-fit on F^2	1.172
Final R indices	2611 data; I>2σ(I) R1 = 0.0729, wR2 = 0.1728
	all data R1 = 0.0997, wR2 = 0.1909
Weighting scheme	$w=1/[\sigma^2(F_o^2)+(0.0881P)^2+0.3300P]$ where $P=(F_o^2+2F_c^2)/3$
Largest diff. peak and hole	1.525 and -0.575 eÅ^{-3}
R.M.S. deviation from mean	0.169 eÅ^{-3}

Table S2. Data collection and structure refinement for $(CH_3\text{-}(CH_2)_{n-1}\text{-}NH_3)_2MnCl_4$ (n=10) at 308 K.

Theta range for data collection	0.76 to 28.35°
Index ranges	-35<=h<=34, -9<=k<=9, -9<=l<=9
Reflections collected	14408
Independent reflections	3517 [R(int) = 0.0766]
Coverage of independent reflections	99.4%
Absorption correction	Multi-Scan
Structure solution technique	direct methods
Structure solution program	XT, VERSION 2014/5
Refinement method	Full-matrix least-squares on F^2
Refinement program	SHELXL-2014/7 (Sheldrick, 2014)
Function minimized	$\Sigma\ w(F_o^2 - F_c^2)^2$
Data / restraints / parameters	3517 / 9 / 134
Goodness-of-fit on F^2	1.137
Final R indices	2583 data; I>2σ(I) R1 = 0.0698, wR2 = 0.1743
	all data R1 = 0.1019, wR2 = 0.2000
Weighting scheme	$w=1/[\sigma^2(F_o^2)+(0.1002P)^2+0.5556P]$ where $P=(F_o^2+2F_c^2)/3$
Absolute structure parameter	0.00(9)
Largest diff. peak and hole	1.459 and -0.684 eÅ^{-3}
R.M.S. deviation from mean	0.181 eÅ^{-3}

Table S3. Data collection and structure refinement for $(CH_3-(CH_2)_{n-1}-NH_3)_2MnCl_4$ (n=10) at 320 K.

|	
Theta range for data collection	1.42 to 27.99°
Index ranges	-6<=h<=6, -6<=k<=5, -32<=l<=36
Reflections collected	2061
Independent reflections	601 [R(int) = 0.1034]
Coverage of independent reflections	92.3%
Absorption correction	Multi-Scan
Structure solution technique	direct methods
Structure solution program	XT, VERSION 2014/5
Refinement method	Full-matrix least-squares on F^2
Refinement program	SHELXL-2014/7 (Sheldrick, 2014)
Function minimized	$\Sigma\, w(F_o^2 - F_c^2)^2$
Data / restraints / parameters	601 / 0 / 9
Goodness-of-fit on F^2	1.018
Final R indices	342 data; I>2σ(I) R1 = 0.1139, wR2 = 0.2713
	all data R1 = 0.1577, wR2 = 0.3235
Weighting scheme	$w=1/[\sigma^2(F_o^2)+(0.2000P)^2]$ where $P=(F_o^2+2F_c^2)/3$
Absolute structure parameter	0.00(9)
Largest diff. peak and hole	3.171 and -0.620 eÅ^{-3}
R.M.S. deviation from mean	0.148 eÅ^{-3}
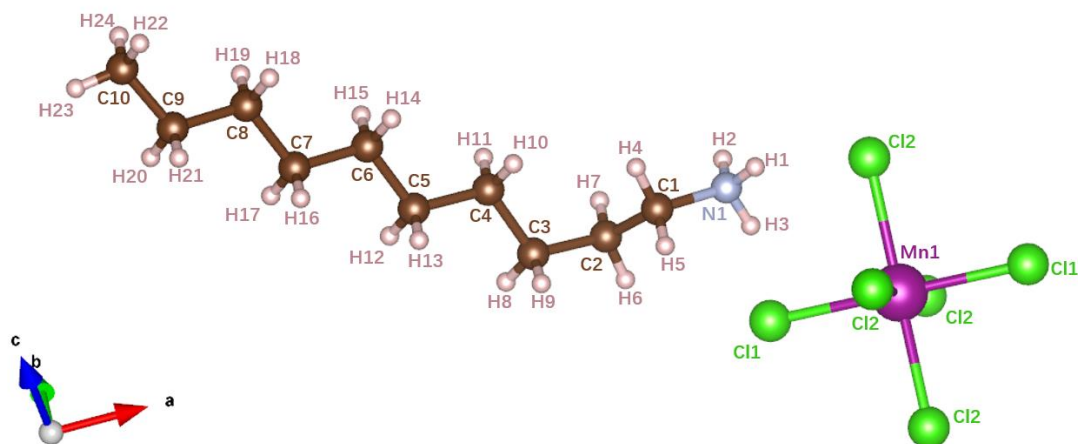
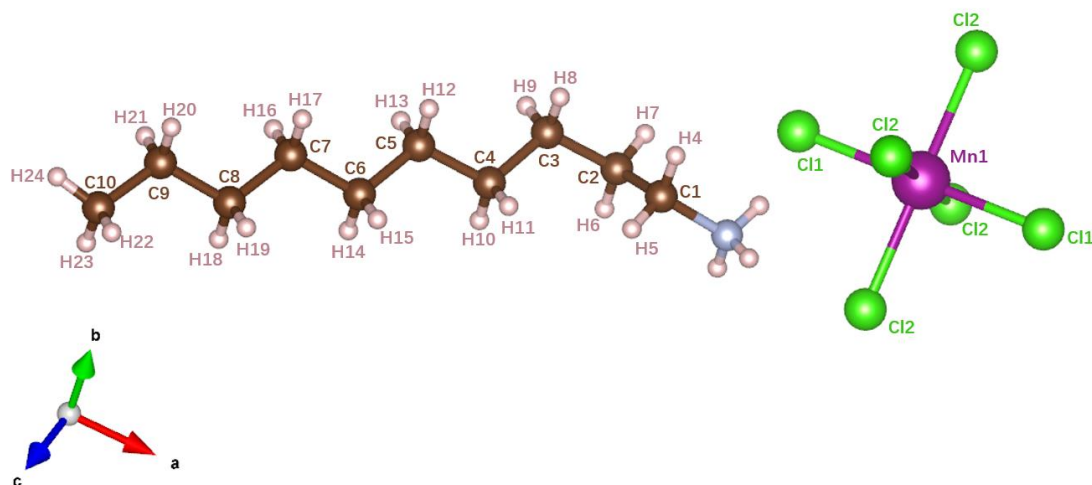**Fig. S2.** Atomic sequence in $(CH_3-(CH_2)_{n-1}-NH_3)_2MnCl_4$ (n=10) at 298 K of low-temperature phase.

Fig. S3. Atomic sequence in $(CH_3\text{-}(CH_2)_{n-1}\text{-}NH_3)_2MnCl_4$ (n=10) at 308 K of low-temperature phase.
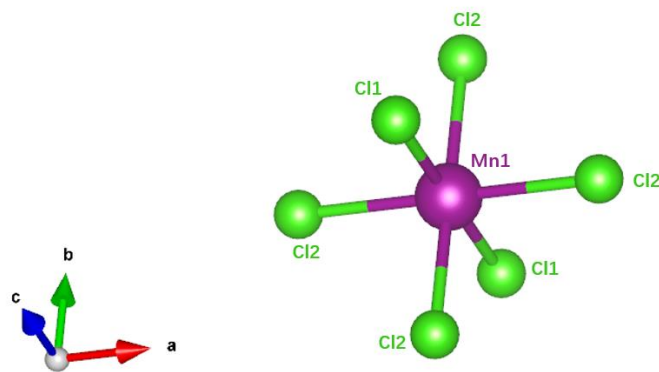

Fig. S4. Atomic sequence in $(CH_3\text{-}(CH_2)_{n-1}\text{-}NH_3)_2MnCl_4$ (n=10) at 320 K of high-temperature phase.

Table S4. Bond angles (°) for $(CH_3\text{-}(CH_2)_{n-1}\text{-}NH_3)_2MnCl_4$ (n=10) at 298 K of low-temperature phase (see Fig. S2).

bond	Angle(°)	bond	Angle(°)
Cl1-Mn1-Cl1	180	Cl1-Mn1-Cl2	89.10(3)
Cl1-Mn1-Cl2	90.90(3)	Cl1-Mn1-Cl2	90.90(3)
Cl1-Mn1-Cl2	89.10(3)	Cl2-Mn1-Cl2	180.00(5)
Cl1-Mn1-Cl2	88.30(3)	Cl1-Mn1-Cl2	91.70(3)
Cl2-Mn1-Cl2	91.610(11)	Cl2-Mn1-Cl2	88.390(12)
Cl1-Mn1-Cl2	91.70(3)	Cl1-Mn1-Cl2	88.30(3)
Cl2-Mn1-Cl2	88.390(11)	Cl2-Mn1-Cl2	91.610(12)
Cl2-Mn1-Cl2	180	N1-C1-C2	112.6(4)
N1-C1-H4	109.1	C2-C1-H4	109.1
N1-C1-H5	109.1	C2-C1-H5	109.1
H4-C1-H5	107.8	Mn1-Cl2-Mn1	166.24(5)
C1-N1-H1	114.(2)	C1-N1-H2	112.(2)
H1-N1-H2	105.(3)	C1-N1-H3	114.(2)
H1-N1-H3	107.(3)	H2-N1-H3	105.(3)
C5-C4-C3	114.3(5)	C5-C4-H10	108.7

bond	Angle(°)	bond	Angle(°)
C3-C4-H10	108.7	C5-C4-H11	108.7
C3-C4-H11	108.7	H10-C4-H11	107.6
C7-C6-C5	114.0(6)	C7-C6-H14	108.7
C5-C6-H14	108.7	C7-C6-H15	108.7
C5-C6-H15	108.7	H14-C6-H15	107.6
C6-C7-C8	115.1(6)	C6-C7-H16	108.5
C8-C7-H16	108.5	C6-C7-H17	108.5
C8-C7-H17	108.5	H16-C7-H17	107.5
C6-C5-C4	115.6(5)	C6-C5-H12	108.4
C4-C5-H12	108.4	C6-C5-H13	108.4
C4-C5-H13	108.4	H12-C5-H13	107.4
C4-C3-C2	116.0(5)	C4-C3-H8	108.3
C2-C3-H8	108.3	C4-C3-H9	108.3
C2-C3-H9	108.3	H8-C3-H9	107.4
C9-C8-C7	114.4(7)	C9-C8-H18	108.7
C7-C8-H18	108.7	C9-C8-H19	108.7
C7-C8-H19	108.7	H18-C8-H19	107.6
C1-C2-C3	111.4(5)	C1-C2-H4	109.3
C3-C2-H4	109.3	C1-C2-H5	109.3
C3-C2-H5	109.3	H4-C2-H5	108
C10-C9-C8	116.3(8)	C10-C9-H20	108.2
C8-C9-H20	108.2	C10-C9-H21	108.2
C8-C9-H21	108.2	H20-C9-H21	107.4
C9-C10-H22	109.5	C9-C10-H23	109.5
H22-C10-H23	109.5	C9-C10-H24	109.5
H22-C10-H24	109.5	H23-C10-H24	109.5

Table S5. Bond angles (°) for $(CH_3-(CH_2)_{n-1}-NH_3)_2MnCl_4$ (n=10) at 308 K of low-temperature phase (see Fig. S3).

bond	Angle(°)	bond	Angle(°)
Cl1-Mn1-Cl1	180	Cl1-Mn1-Cl2	90.86(3)
Cl1-Mn1-Cl2	89.14(3)	Cl1-Mn1-Cl2	89.14(3)
Cl1-Mn1-Cl2	90.86(3)	Cl2-Mn1-Cl2	180
Cl1-Mn1-Cl2	88.43(3)	Cl1-Mn1-Cl2	91.57(3)
Cl2-Mn1-Cl2	88.403(19)	Cl2-Mn1-Cl2	91.597(19)
Cl1-Mn1-Cl2	91.57(3)	Cl1-Mn1-Cl2	88.43(3)
Cl2-Mn1-Cl2	91.597(19)	Cl2-Mn1-Cl2	88.40(2)
Cl2-Mn1-Cl2	180.00(2)	C1-N1-H1	113.(2)
C1-N1-H2	112.(2)	H1-N1-H2	107.(3)
C1-N1-H3	112.(2)	H1-N1-H3	107.(3)
H2-N1-H3	105.(3)	N1-C1-C2	113.3(5)
N1-C1-H4	108.9	C2-C1-H4	108.9
N1-C1-H5	108.9	C2-C1-H5	108.9
H4-C1-H5	107.7	Mn1-Cl2-Mn1	166.58(5)
C5-C4-C3	114.6(6)	C5-C4-H10	108.6
C3-C4-H10	108.6	C5-C4-H11	108.6
C3-C4-H11	108.6	H10-C4-H11	107.6
C1-C2-C3	112.3(5)	C1-C2-H6	109.1
C3-C2-H6	109.1	C1-C2-H7	109.1
C3-C2-H7	109.1	H6-C2-H7	107.9
C7-C6-C5	114.3(6)	C7-C6-H14	108.7
C5-C6-H14	108.7	C7-C6-H15	108.7
C5-C6-H15	108.7	H14-C6-H15	107.6

bond	Angle(°)	bond	Angle(°)
C6-C5-C4	116.0(6)	C6-C5-H12	108.3
C4-C5-H12	108.3	C6-C5-H13	108.3
C4-C5-H13	108.3	H12-C5-H13	107.4
C4-C3-C2	116.1(6)	C4-C3-H8	108.3
C2-C3-H8	108.3	C4-C3-H9	108.3
C2-C3-H9	108.3	H8-C3-H9	107.4
C6-C7-C8	115.8(7)	C6-C7-H16	108.3
C8-C7-H16	108.3	C6-C7-H17	108.3
C8-C7-H17	108.3	H16-C7-H17	107.4
C9-C8-C7	115.2(7)	C9-C8-H18	108.5
C7-C8-H18	108.5	C9-C8-H19	108.5
C7-C8-H19	108.5	H18-C8-H19	107.5
C10-C9-C8	116.7(9)	C10-C9-H20	108.1
C8-C9-H20	108.1	C10-C9-H21	108.1
C8-C9-H21	108.1	H20-C9-H21	107.3
C9-C10-H22	109.5	C9-C10-H23	109.5
H22-C10-H23	109.5	C9-C10-H24	109.5
H22-C10-H24	109.5	H23-C10-H24	109.5

Table S6. Bond angles (°) for $(CH_3-(CH_2)_{n-1}-NH_3)_2MnCl_4$ (n=10) at 320 K of high-temperature phase (see Fig. S4).

bond	Angle(°)	bond	Angle(°)
Mn1-Cl2-Mn1	180	Cl1-Mn1-Cl1	180
Cl1-Mn1-Cl2	90	Cl1-Mn1-Cl2	90
Cl1-Mn-Cl2	90	Cl1-Mn1-Cl2	90
Cl2-Mn1-Cl2	90	Cl1-Mn1-Cl2	90
Cl1-Mn1-Cl2	90	Cl2-Mn1-Cl2	90
Cl2-Mn1-Cl2	180	Cl1-Mn1-Cl2	90
Cl1-Mn1-Cl2	90	Cl2-Mn1-Cl2	180
Cl2-Mn1-Cl2	90	Cl2-Mn1-Cl2	90

Crystal structural diagram of $(CH_3-(CH_2)_{n-1}-NH_3)_2MnCl_4$ (n=10) at 298K, 308K, and 320K below and above T_s=311.5K are shown in Fig. S5-12. The lattice structural diagrams viewed along different axis are shown respectively for crystal at 298 K (Fig. S5-7), 308 K (Fig. S8-10) of low-temperature phase and 320 K (Fig. S11-12) of high-temperature phase.
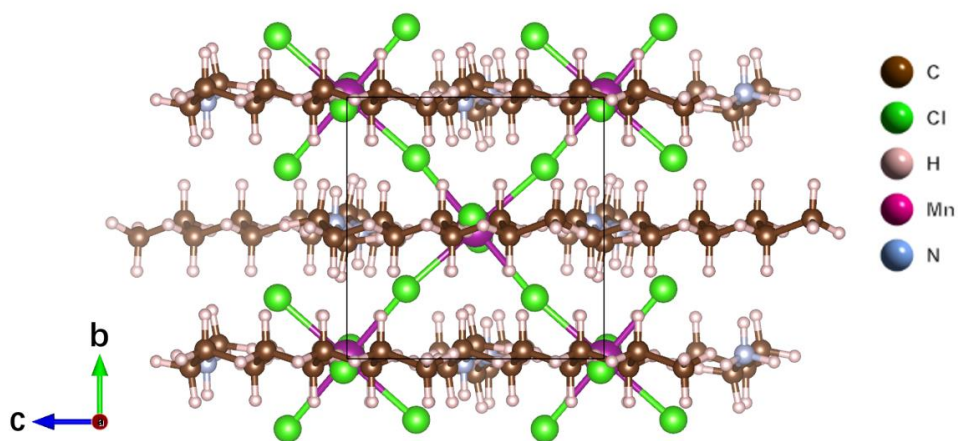
Fig. S5. Structural diagram of $(CH_3\text{-}(CH_2)_{n-1}\text{-}NH_3)_2MnCl_4$ (n=10) at 298K of low-temperature phase viewed along a axis.
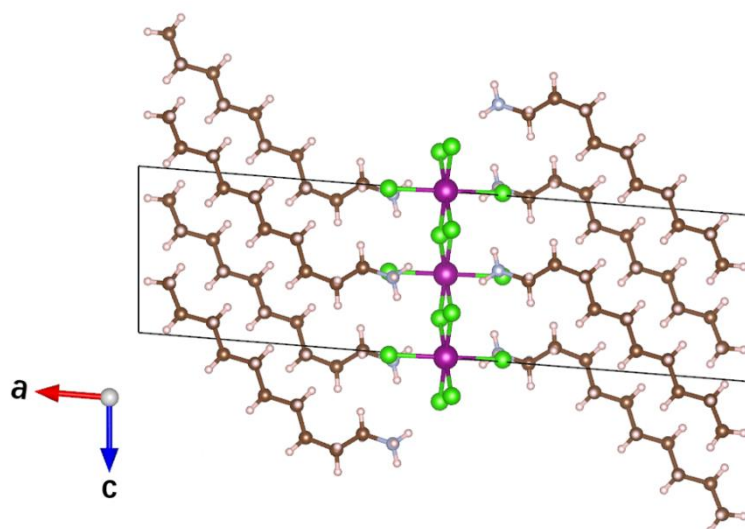

Fig. S6. Structural diagram of $(CH_3\text{-}(CH_2)_{n-1}\text{-}NH_3)_2MnCl_4$ (n=10) at 298 K of low-temperature phase viewed along b axis.
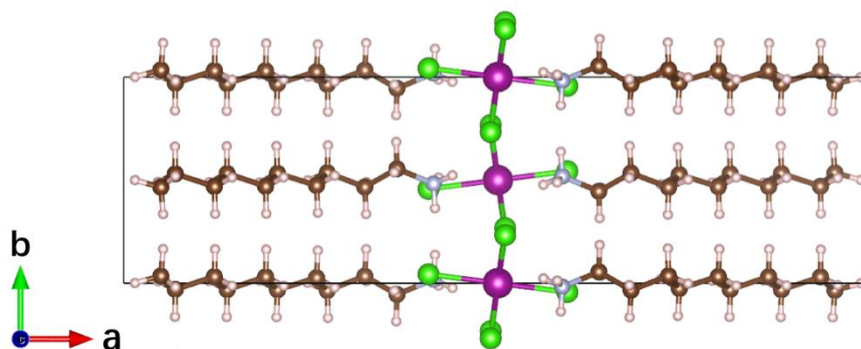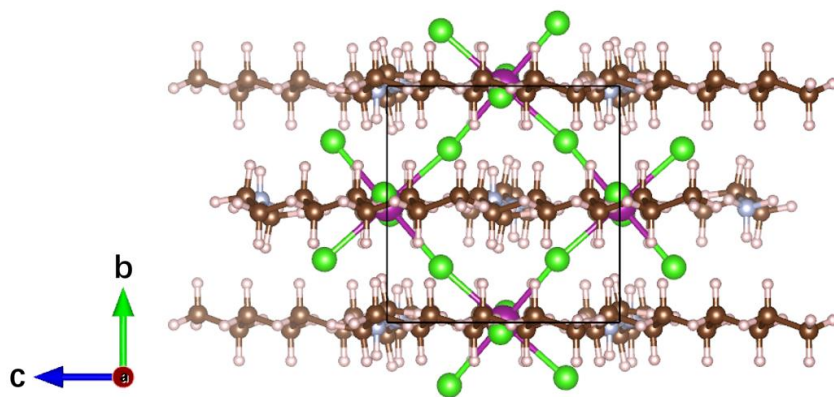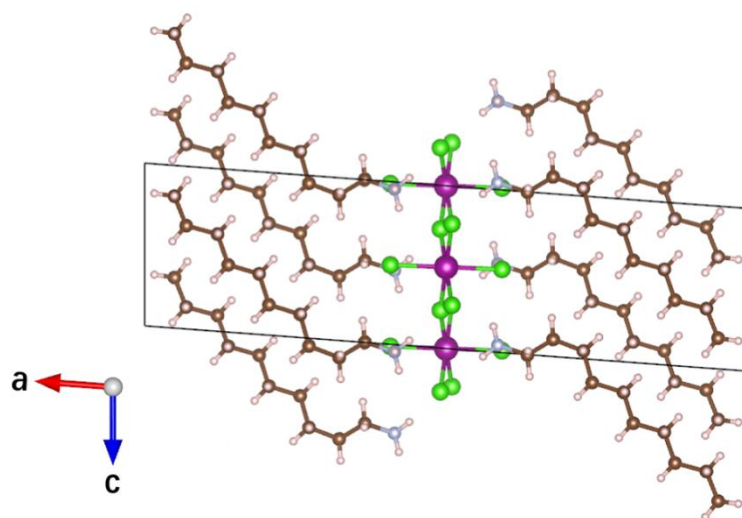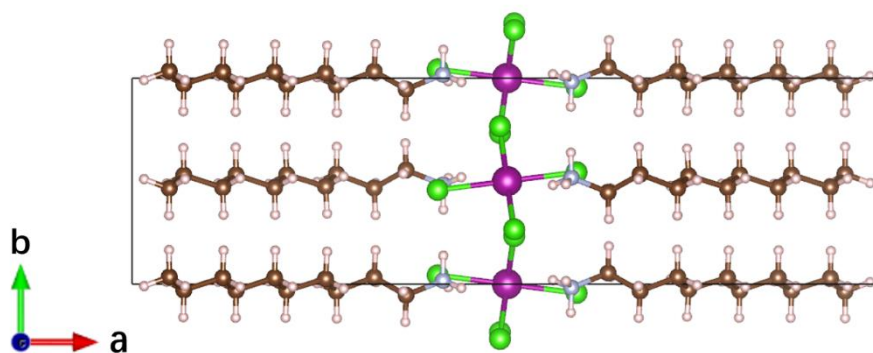

Fig. S7. Structural diagram of $(CH_3\text{-}(CH_2)_{n-1}\text{-}NH_3)_2MnCl_4$ (n=10) at 298 K of low-temperature phase viewed along c axis.

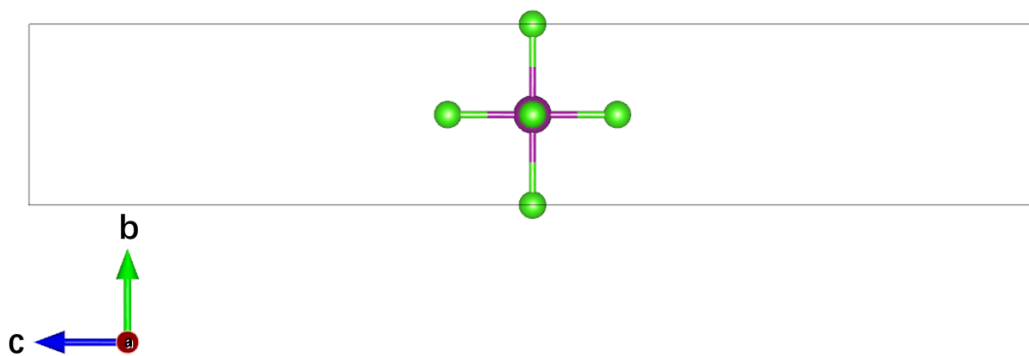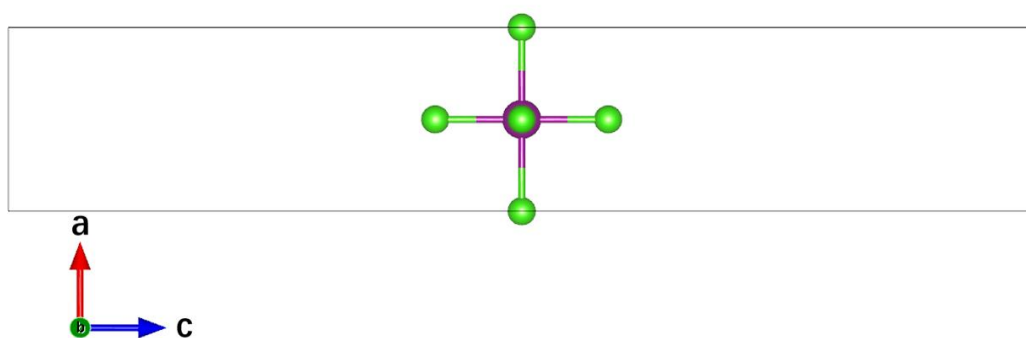**Fig. S8.** Structural diagram of $(CH_3-(CH_2)_{n-1}-NH_3)_2MnCl_4$ (n=10) at 308 K of low-temperature phase viewed along a axis.

Fig. S9. Structural diagram of $(CH_3-(CH_2)_{n-1}-NH_3)_2MnCl_4$ (n=10) at 308 K of low-temperature phase viewed along b axis.

Fig. S10. Structural diagram of $(CH_3-(CH_2)_{n-1}-NH_3)_2MnCl_4$ (n=10) at 308 K of low-temperature phase viewed along c axis.

Fig. S11. Structural diagram of $(CH_3\text{-}(CH_2)_{n-1}\text{-}NH_3)_2MnCl_4$ (n=10) at 320 K of high-temperature phase viewed along a axis.

Fig. S12. Structural diagram of $(CH_3\text{-}(CH_2)_{n-1}\text{-}NH_3)_2MnCl_4$ (n=10) at 320 K of high-temperature phase viewed along b axis.
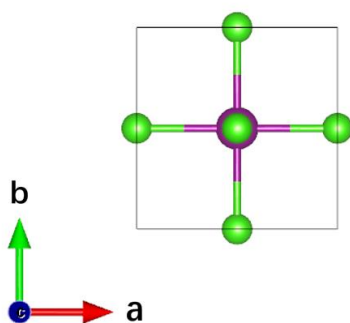

Fig. S13. Structural diagram of $(CH_3\text{-}(CH_2)_{n-1}\text{-}NH_3)_2MnCl_4$ (n=10) at 320 K of high-temperature phase viewed along c axis.

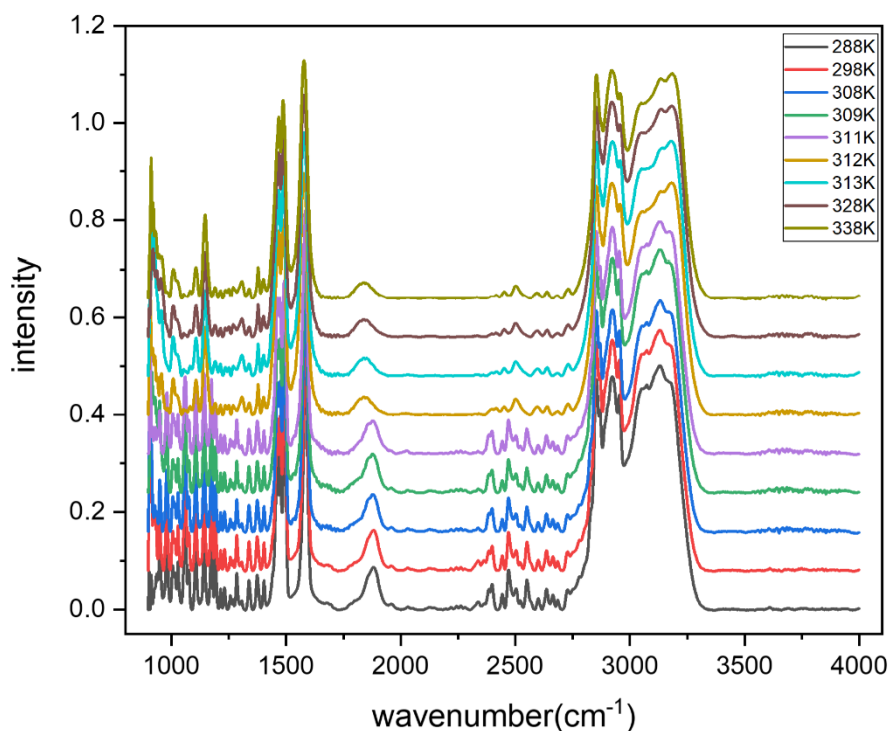## SI-3. Fourier transform infrared spectroscopy measurements of $(CH_3\text{-}(CH_2)_{n-1}\text{-}NH_3)_2MnCl_4$ (n=10)

Fig. S14. Infrared spectra of $(CH_3\text{-}(CH_2)_{n-1}\text{-}NH_3)_2MnCl_4$ (n=10) at variable temperatures from 288 K to 338 K on heating.

Using a BRUKER TENSOR II FTIR (Fourier Transform Infrared) spectrometer, we performed infrared (IF) spectroscopy on $(CH_3\text{-}(CH_2)_{n-1}\text{-}NH_3)_2MnCl_4$ (n=10) in the frequency range of 900-4000 cm^{-1} with 1.5 cm^{-1} resolution. Fig. S14 shows complete IR spectrogram of single crystal $(CH_3\text{-}(CH_2)_9\text{-}NH_3)_2MnCl_4$. The specific vibration bands corresponding to the NH_3, CH_2, and CH_3 groups and C-C chains from head to tail in the entire $(CH_3\text{-}(CH_2)_9\text{-}NH_3)^+$ organic chain are given in Fig. 3 of main text. The bands at 298 K and corresponding assignments are listed in Table S7.

Table S7. IR bands and the vibration assignments of $(CH_3\text{-}(CH_2)_{n-1}\text{-}NH_3)_2MnCl_4$ (n=10) at 298 K are listed.

V_{IR} (cm^{-1})	intensity	assignment
1143	m	$\omega(CH_2)$
1175	m	$\omega(CH_2)$
1374	m	$\sigma_s(CH_3)$
1462	s	$\delta(CH_2)$
1474	s	$\delta(CH_2)$
1494	s	$\sigma_s(NH_3)$
1585	vs	$\sigma_{as}(NH_3)$
1881	m	$C\text{-}NH_3^+$
2853	vs	$\nu_s(CH_2)$
2868	s	$\nu_s(CH_3)$
2923	vs	$\nu_{as}(CH_2)$
2953	s	$\nu_{as}(CH_3)$

| 3074 | s | $\nu(NH_3)$ |
| 3131 | vs | $\nu(NH_3)$ |

(ν = stretching, σ = bending; ρ = rocking; δ = scissoring; ω = wagging; τ = twisting; . as = asymmetric; s = symmetric. vs = very strong; s = strong; m = medium.)

SI-4. Barocaloric characterization on $(CH_3\text{-}(CH_2)_{n\text{-}1}\text{-}NH_3)_2MnCl_4$ (n=9)

In analogy to $(CH_3\text{-}(CH_2)_{n\text{-}1}\text{-}NH_3)_2MnCl_4$ (n=10), the close composition $(CH_3\text{-}(CH_2)_{n\text{-}1}\text{-}NH_3)_2MnCl_4$ (n=9) with one reduced CH_2 in each organic chain also exhibits great barocaloric performance. For the hybrid organic-inorganic layer perovskite $(CH_3\text{-}(CH_2)_{n\text{-}1}\text{-}NH_3)_2MX_4$ with long organic chains (n ⩾ 9),[S1-2] the T_s (phase transition temperature) shows rising with increasing n. T_s (on heating) of $(CH_3\text{-}(CH_2)_{n\text{-}1}\text{-}NH_3)_2MnCl_4$ (n=9) is identified as ~294.3 K, closely near room temperature (Fig. S15). Notably, Fig. S15 indicates two phase transitions occurring in sequence with temperature changing in $(CH_3\text{-}(CH_2)_{n\text{-}1}\text{-}NH_3)_2MnCl_4$ (n=9). According to previous literature[S3-4], the major phase transition is accompanied by the conformational order-disorder transition of organic chains, and the minor phase transition is relevant to rotational order-disorder transition of organic chains around the longitudinal chain axis.

Measurements of high pressure DSC (Fig. S16) show that phase transition temperature increases significantly with pressure increasing, roughly at the rate of 172 K GPa^{-1}. Moreover, under atmosphere pressure, two phase transitions are separated, while increasing pressure to 0.02 GPa or further increasing, phase transition is finished in one step all along. It is indicated that under moderate pressure, two transitions, related to conformation disorder and rotational disorder of organic chains respectively, get interconnected tightly and triggered by each other. Fig. S17 presents the stable and colossal latent entropy change ~212 J kg^{-1} K^{-1} under 0–0.1 GPa, and when considering specific heat-induced entropy, correspondence between S, T and P can be shown in Fig. S18. Utilizing quasi-direct method aforementioned, barocaloric performance of $(CH_3\text{-}(CH_2)_{n\text{-}1}\text{-}NH_3)_2MnCl_4$ (n=9) is evaluated. It is indicated that the largest ΔS_P of 212 J kg^{-1} K^{-1} is achieved under pressure of 0.06 GPa(Fig. S19) and ΔT_P of 14 K is achieved under pressure of 0.1 GPa (Fig. S20). Moreover, under applied pressure of 0.08 GPa, the reversible ΔS_r reaches the maximum 212 J kg^{-1} K^{-1} (Fig. S21), and ΔT_r reaches 10 K (Fig. S22) under pressure of 0.1 GPa. Also, the specific heat capacity curve for $(CH_3\text{-}(CH_2)_{n\text{-}1}\text{-}NH_3)_2MnCl_4$ (n=9) is shown in Fig. S24.

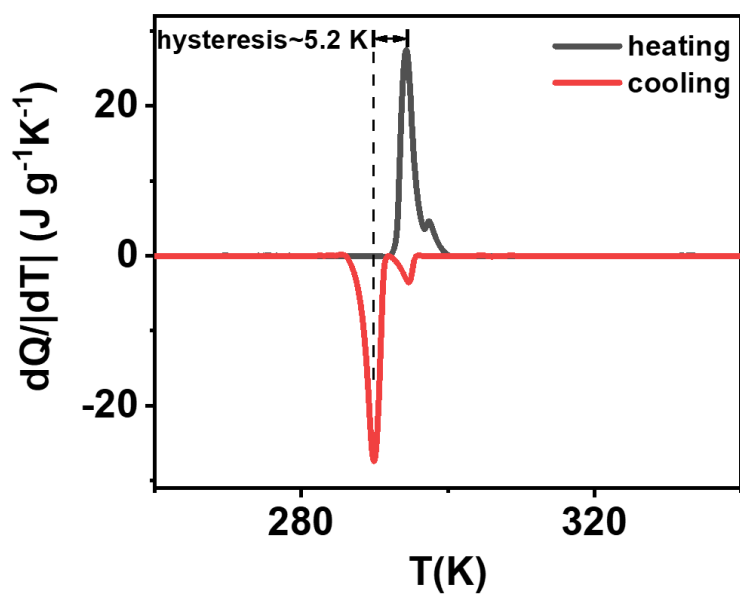**Fig. S15.** Heat flow vs T curve under atmosphere pressure in $(CH_3\text{-}(CH_2)_{n\text{-}1}\text{-}NH_3)_2MnCl_4$ (n=9) with temperature rate 1K/min.
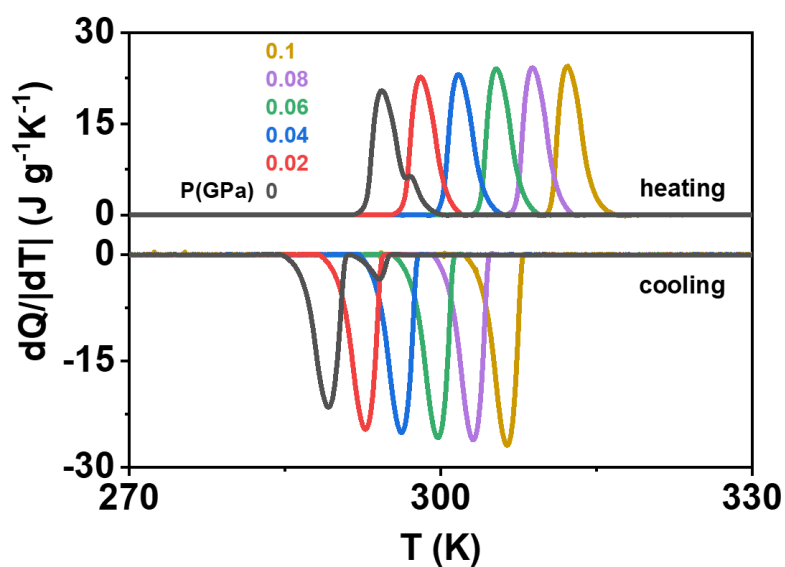

Fig. S16. Isobaric heat flow curves under 0-0.1 GPa in $(CH_3\text{-}(CH_2)_{n\text{-}1}\text{-}NH_3)_2MnCl_4$ (n=9) measured with temperature rate 1K/min.
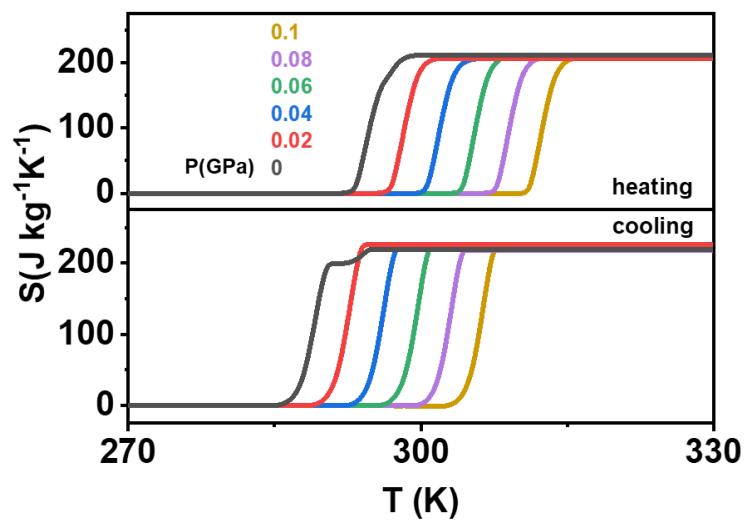
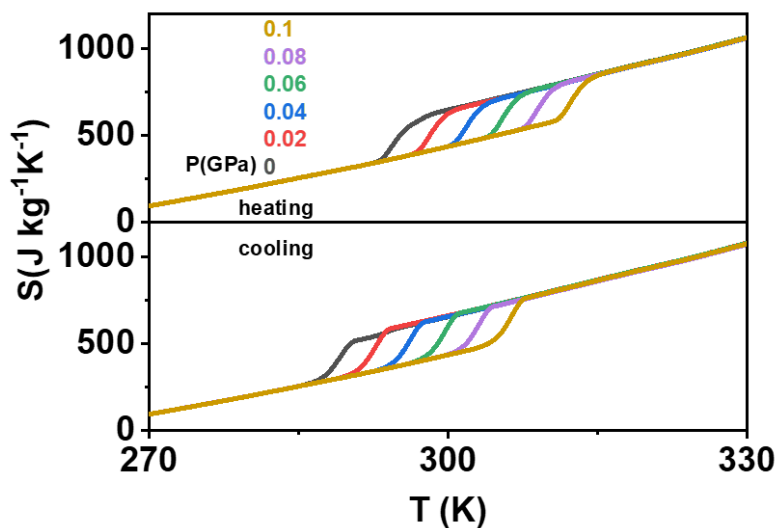**Fig. S17.** Isobaric entropy calculated from isobaric heat flow curves in $(CH_3-(CH_2)_{n-1}-NH_3)_2MnCl_4$ (n=9).

Fig. S18. Isobaric entropy curves adding specific heat entropy in $(CH_3-(CH_2)_{n-1}-NH_3)_2MnCl_4$ (n=9).

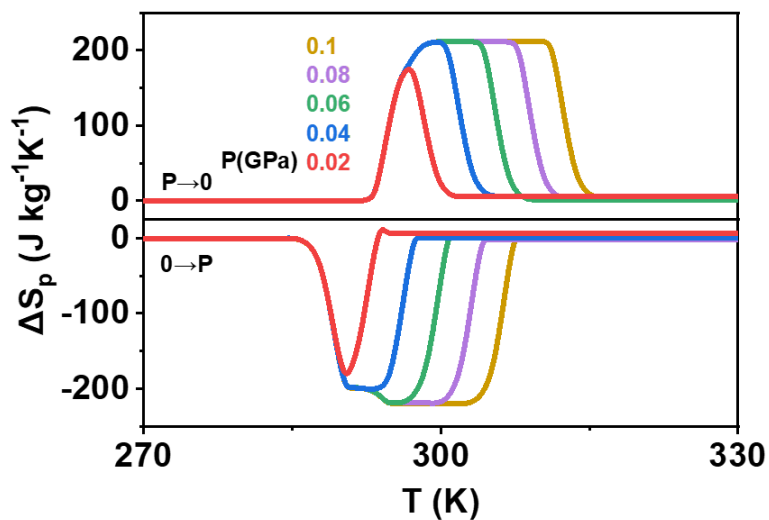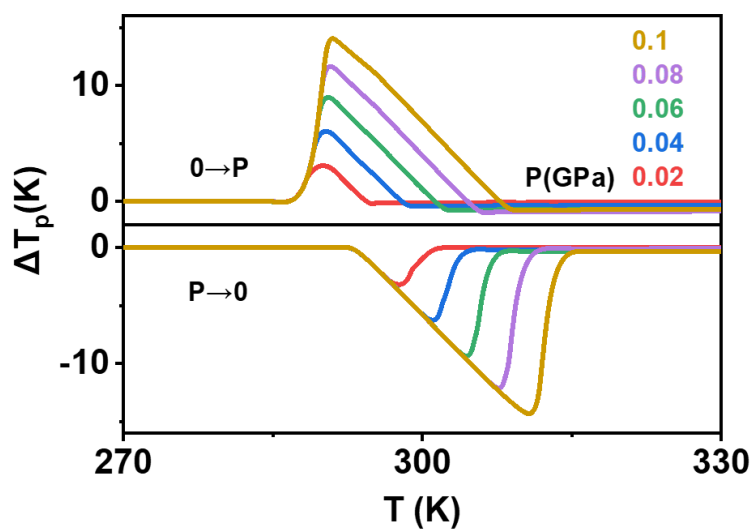**Fig. S19.** Pressure-induced isothermal entropy change in $(CH_3\text{-}(CH_2)_{n-1}\text{-}NH_3)_2MnCl_4$ (n=9).

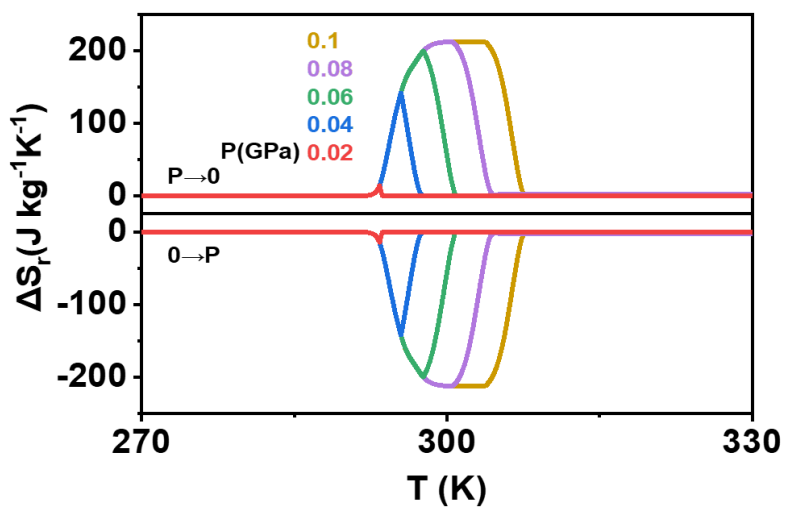**Fig. S20.** Pressure-induced adiabatic temperature change in $(CH_3\text{-}(CH_2)_{n-1}\text{-}NH_3)_2MnCl_4$ (n=9).

Fig. S21. Pressure-induced reversible isothermal entropy change in $(CH_3\text{-}(CH_2)_{n-1}\text{-}NH_3)_2MnCl_4$ (n=9).

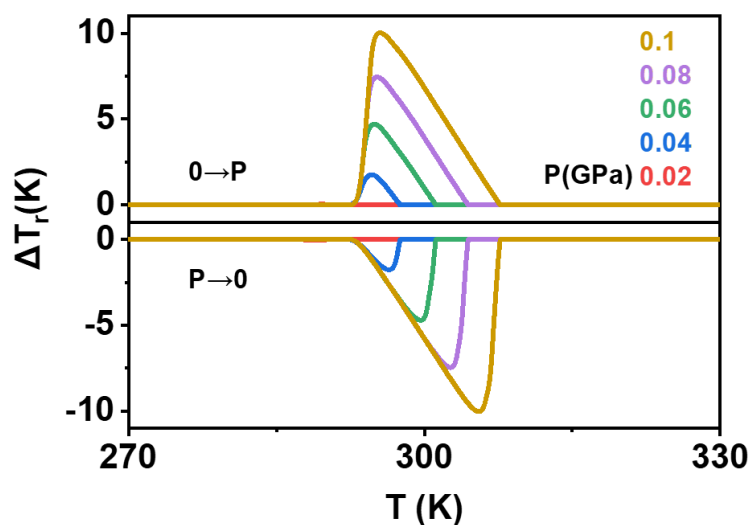**Fig. S22.** Pressure-induced reversible adiabatic temperature change in $(CH_3-(CH_2)_{n-1}-NH_3)_2MnCl_4$ (n=9).

SI-5. Characterization of barocaloric performance by quasi-direct method

Isobaric calorimetry data were obtained with μDSC7 evo microcalorimeter from SETARAM. Specifically, the applied pressure from 0-0.1GPa is formed by compressed gas. Under constant pressure, the differential scanning calorimetry is performed on samples. Fig. S23 shows the entropy calculated from isobaric heat flow curves (Fig. 5a) when not adding entropy from specific heat for $(CH_3-(CH_2)_{n-1}-NH_3)_2MnCl_4$ (n=10) single crystal. It is exhibited explicitly that with pressure increasing, complete phase transition can still be driven thermally with almost undiminished entropy change $\sim$230 J kg^{-1} K^{-1}.

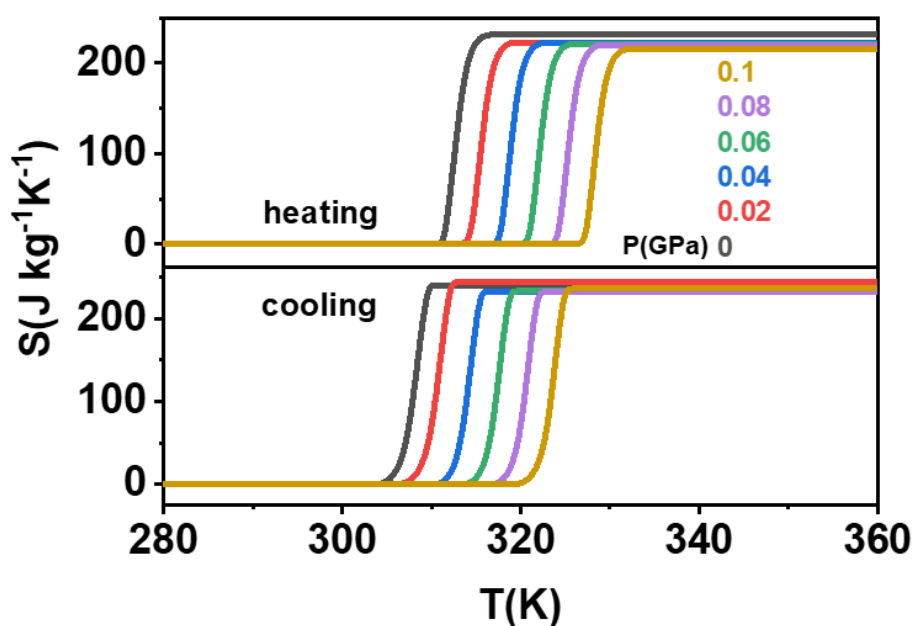**Fig. S23.** Entropy change of $(CH_3-(CH_2)_{n-1}-NH_3)_2MnCl_4$ (n=10) single crystal calculated from

isobaric heat flow curve.

When considering specific heat, the correspondence between entropy (S), pressure (P) and temperature (T) is established by formula below:[S5]

$$S(T,P) = S(T_0,P) + \int_{T_0}^{T} \frac{1}{T'} \left(\frac{dQ(T',P)}{dT'} + C_p(T',P) \right) dT'$$

Wherein, for appropriately selected T_0, S (T_0, P) is for reference as 0 J kg^{-1} K^{-1}. C_p (T', P) is approximately determined as C_p(T') under atmosphere pressure.

Quasi-direct method is used to measure barocaloric performance.[S5-6] Isothermal entropy change (ΔS_p) and adiabatic temperature change (ΔT_p) induced by pressure change of ΔP are evaluated via $\Delta S_p(\Delta P,T) = S(P_0 + \Delta P,T) - S(P_0,T)$ and $\Delta T_p(\Delta P,S) = T(P_0 + \Delta P,S) - T(P_0,S)$. Specifically, for eliminating error from hysteresis, pressurization-induced $\Delta S_p(\Delta P,T)$ and $\Delta T_p(\Delta P,S)$, that is $\Delta P > 0$, should be obtained from S(P,T) (and T(P,S)) curves on cooling, and depressurization-induced $\Delta S_p(\Delta P,T)$ and $\Delta T_p(\Delta P,S)$, that is $\Delta P < 0$, should be obtained from S(P,T) (and T(P,S)) curves on heating.

Moreover, the reversible isothermal entropy change (ΔS_r) is reckoned as the overlapping of ΔS_p on compression and decompression, while similarly the reversible adiabatic temperature change (ΔT_r) is obtained excluding the influence of thermal hysteresis. [S7-8]

SI-6. Specific heat capacity of (CH$_3$-(CH$_2$)$_{n-1}$-NH$_3$)$_2$MnCl$_4$

The specific heat capacity of (CH$_3$-(CH$_2$)$_{n-1}$-NH$_3$)$_2$MnCl$_4$ (n=10 single crystal, and n=9 sample) were measured by micro calorimeter (μDSC7 evo microcalorimeter, SETARAM, France) at atmosphere pressure in our experiments, as shown in Fig. S24 and Fig. S25, where the solid base line neglecting latent heat of phase transition was used to calculate the entropy curves. For completeness, the entropy curves with the specific heat capacity included and not are also given together.
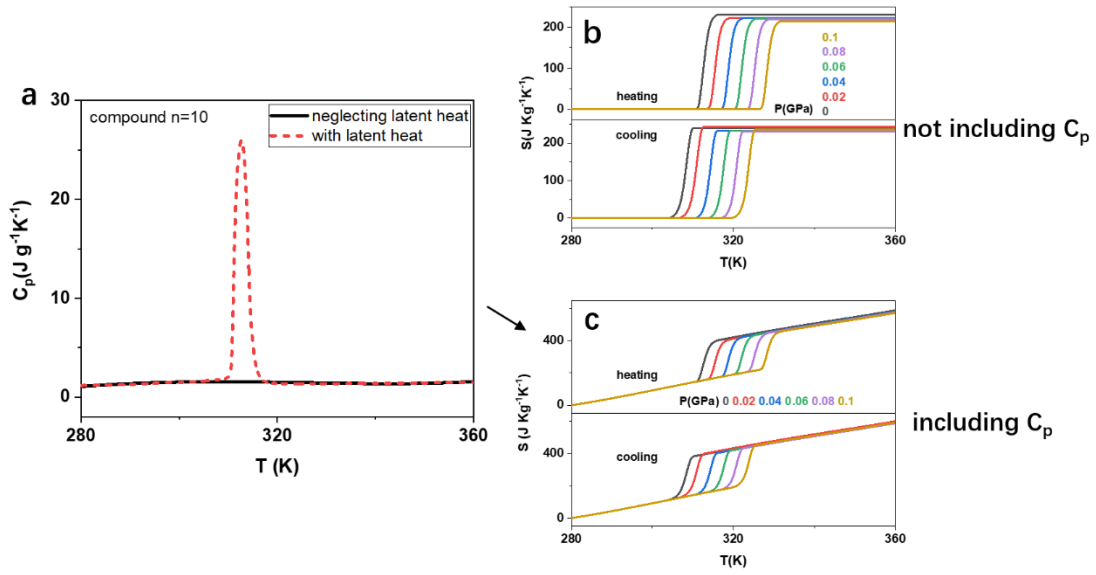
Fig. S24. a) The measured specific heat capacity vs. temperature for $(CH_3\text{-}(CH_2)_{n-1}\text{-}NH_3)_2MnCl_4$ (n=10) single ccystal, where the solid base line neglecting latent heat of phase transition was used to calculate the entropy curves. For completeness, the entropy curves without b) and with c) the specific heat capacity included are also given together.

Fig. S25. a) The measured specific heat capacity vs. temperature for $(CH_3\text{-}(CH_2)_{n-1}\text{-}NH_3)_2MnCl_4$ (n=9), where the solid base line neglecting latent heat of phase transition was used to calculate the entropy curves. For completeness, the entropy curves without b) and with c) the specific heat capacity included are also given together.
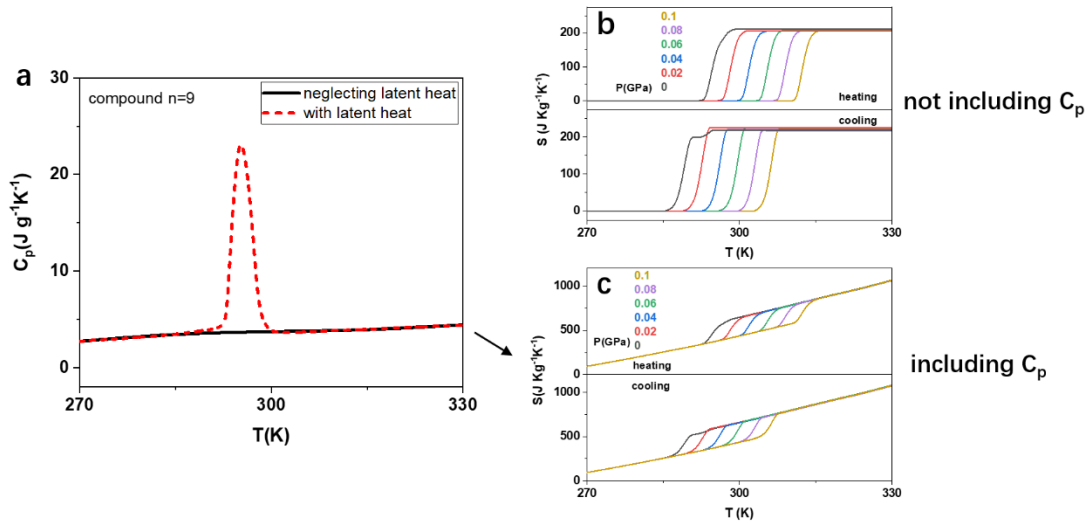
SI-7. Additional barocaloric effect in $(CH_3\text{-}(CH_2)_{n-1}\text{-}NH_3)_2MnCl_4$ (n=10)

On the basis of Maxwell relation $\left(\frac{dV}{dT}\right)_P = \left(\frac{dS}{dP}\right)_T$, if we approximately regard $\left(\frac{dV}{dT}\right)_P$ as $\left(\frac{dV}{dT}\right)_{P=0}$, the additional barocaloric entropy change beyond the transition can be described as $\Delta S = \left(\frac{dV}{dT}\right)_{P=0} \cdot \Delta P$.

According to the V-T values at atmosphere pressure available in literature [25] for

$(CH_3-(CH_2)_{n-1}-NH_3)_2MnCl_4$ (n=10)[S9], at low temperature around 280K away from phase transition Ts=310K, $\left(\frac{dV}{dT}\right)_{P=0}$ can be estimated to be 0.0438 $Å^3$ K^{-1} per unit cell. Then the additional barocaloric entropy change under pressure of 0.1 GPa is estimated to be ~2.6 J kg^{-1} K^{-1}, which is neglectable small compared to the colossal barocaloric entropy change ΔS=230 J kg^{-1} K^{-1} from phase transition under the same pressure of 0.1 GPa.

References:

S1. Vacatello, M., Corradini, P., Relationships between structure and properties of compounds of the type $(RNH_3)_2MX_4$, II. Compounds with M=Mn, X=Cl and R=n-C_9H_{19}, n-$C_{11}H_{23}$, n-$C_{13}H_{27}$, n-$C_{15}H_{31}$ and n-$C_{17}H_{35}$. *Gazz. Chim. Ital.* **104**, 773-780 (1974).

S2. Vacatello, M., *Ann. Chim. (Rome, Italy)* **64**, 13-18 (1974).

S3. Kind, R., Plesko, S., Gunter, P., Roos, J., Fousek, J., *Phys. Rev. B: Condens. Matter* **23**, 5301 (1981).

S4. Kind, R., Plesko, S., Gunter, P., Roos, J., Fousek, J., *Phys. Rev. B: Condens. Matter* **24**, 4910 (1981).

S5. Manosa, L., Planes, A., Materials with giant mechanocaloric effects: cooling by strength. *Adv. Mater.* **29**, 1603607 (2017).

S6. Moya, X., Kar-Narayan, S., Mathur, N. D., Caloric materials near ferroic phase transitions. *Nature Mater.* **13**, 439-450 (2014).

S7. Aznar, A., Lloveras, P., Romanini, M., Barrio, M., Tamarit, J.-L., Cazorla, C., et al., Giant barocaloric effects over a wide temperature range in superionic conductor AgI. *Nat. Commun.* **8**, 1851 (2017).

S8. Aznar, A., Negrier, P., Planes, A., Mañosa, L., Stern-Taulats, E., Moya, X., et al., Reversible colossal barocaloric effects near room temperature in 1-X-adamantane (X=Cl, Br) plastic crystals. *Applied Materials Today* **23**, 101023 (2021).

S9. Li, J., Barrio, M., Dunstan, D. J., Dixey, R., Lou, X., Tamarit, J. L., et al., Colossal reversible barocaloric effects in layered hybrid perovskite $(C_{10}H_{21}NH_3)_2MnCl_4$ under low pressure near room temperature. *Adv. Funct. Mater.* 2105154 (2021).